Received: 13 February 2024 | Revised: 19 April 2024 | Accepted: 24 April 2024

DOI: 10.1002/jcc.27434

RESEARCH ARTICLE

Journal of COMPUTATIONAL CHEMISTRY WILEY

Effective prediction of SnO_2 conduction band edge potential: The key role of surface oxygen vacancies

Gennaro Vincenzo Sannino[1] | Adriana Pecoraro[2] | Paola Delli Veneri[3] | Michele Pavone[1] | Ana Belén Muñoz-García[2]

[1]Department of Chemical Sciences, University of Naples Federico II, Naples, Italy

[2]Department of Physics "E. Pancini", University of Naples Federico II, Naples, Italy

[3]Italian National Agency for New Technologies, Energy and Sustainable Economic Development (ENEA), Portici, Italy

Correspondence
Michele Pavone, Department of Chemical Sciences, University of Naples Federico II, Naples, Italy.
Email: michele.pavone@unina.it

Ana Belén Muñoz-García, Department of Physics "E. Pancini", University of Naples Federico II, Naples, Italy.
Email: anabelen.munozgarcia@unina.it

Funding information
European Union Next-Generation EU (PIANO NAZIONALE DI RIPRESA E RESILIENZA (PNRR)—MISSIONE 4 COMPONENTE 2, INVESTIMENTO 1.3)

Abstract

Several theoretical studies at different levels of theory have attempted to calculate the absolute position of the SnO_2 conduction band, whose knowledge is key for its effective application in optoelectronic devices such us, for example, perovskite solar cells. However, the predicted band edges fall outside the experimentally measured range. In this work, we introduce a computational scheme designed to calculate the conduction band minimum values of SnO_2, yielding results aligned with experiments. Our analysis points out the fundamental role of encompassing surface oxygen vacancies to properly describe the electronic profile of this material. We explore the impact of both bridge and in-plane oxygen vacancy defects on the structural and electronic properties of SnO_2, explaining from an atomistic perspective the experimental observables. The results underscore the importance of simulating both types of defects to accurately predict SnO_2 features and provide new fundamental insights that can guide future studies concerning design and optimization of SnO_2-based materials and functional interfaces.

1 | INTRODUCTION

Metal-oxide semiconductors exhibit versatile properties that find applications in a wide range of technologies, including flat-panel displays,[1–3] gas sensors,[4,5] photodetectors,[6,7] solar cells,[8–10] thin-film transistors[1,11] and catalysis.[12–14] Their outstanding physical and chemical characteristics, combined with cheap and simple preparation methods, promote the widespread use of these materials.

Tin(IV) oxide, also known as stannic oxide (SnO_2), has received significant attention owing to its distinctive feature of being simultaneously transparent and conductive.[15] Although being a wide bandgap material, with bandgap values ranging from 3.5 eV to over 4.0 eV depending on specific synthesis conditions,[16] undoped SnO_2 is considered an n-type semiconductor.[15,17,18] This characteristic is attributed to the presence of oxygen vacancies (V_O) in the crystal lattice,[19,20] which create shallow donor levels near the conduction band[21] and cause the reduction of some Sn(IV) ions to Sn(II) as charge compensation mechanism. The resulting electronic conductivity could then occur through the mobility of electrons from Sn(II) to Sn(IV) sites.[19] The most stable crystallographic phase of SnO_2 is rutile (space group $P4_2/mnm$), where each tin is coordinated with six oxygen ions, while each oxygen is surrounded by three tin ions. The (110) surface is considered from various studies[22,23] the lowest energy surface. This facet contains rows of Sn in both six-fold and five-fold coordination, while the surface oxygen ions are classified as "bridging" or "in-plane," depending on whether they are outside or inside the plane, respectively (Figure S1). Consequently, the surface oxygen vacancies are commonly named according to this distinction.

The concentration of surface oxygen vacancies (V_O) can be controlled through fabrication methods or dopings, encompassing a broad spectrum ranging from 15% to 42%.[24–26] Bonu et al.[24] evaluated the ratio between bridge and in-plane V_O (V_{OB} and V_{OP}, respectively) by comparing peak intensities at specific energies of collected photoluminescence (PL) spectra. They found V_{OP}:V_{OB} ratios of 5:8 and 1:2 for SnO_2 nanoparticles, depending on the synthesis process employed. Deepa et al.[27] confirmed the presence of both V_{OP} and V_{OB} in their undoped SnO_2 nanoparticles using Raman analysis and evaluated a V_{OP}:V_{OB} ratio of ~5:4 via PL.

Numerous investigations have underscored the importance of self-doping via oxygen vacancies in improving the performance of SnO_2 across various applications. This includes enhancing its role as an electron transport layer (ETL) in perovskite solar cells,[20,28] boosting photocatalytic activity,[29–31] and advancing sensing capabilities.[32] The electronic structure of stannic oxide undergoes significant modulation based on the amount and nature of oxygen vacancies.[33] These defects introduce intermediate energy levels within the bandgap,[30] playing a pivotal role in shaping the material's electronic profile and the position of its band edges, so impacting on the effective operation of the desired device. Conduction band minimum (CBM) position is a key factor influencing the electronic transport, the material's ability to participate in redox reactions, its response to light and the ability to facilitate electron–hole pair generation and separation. In perovskite solar cells, where SnO_2 has become the actual benchmark ETL, CBM sets the driving force for extracting electrons from the photo-excited perovskite, while its deep valence band ensures effective hole-blocking. For these reasons CBM position represents a critical parameter in the design and optimization of SnO_2-based materials for diverse technological applications, and the knowledge of band edge positioning and the influencing factors is essential to design custom materials for specific applications.

CBM values are generally extracted by combining data from photoemission spectroscopy (PES) and optical spectroscopy. Due to the high variability of oxygen vacancy concentrations depending on the fabrication method, the data reported in the literature for tin dioxide CB edge range widely from −3.8 to −4.8 eV.[34–41] Therefore, it is crucial to choose synthetic processes that provide band positions compatible with the other materials of the device. However, PES instruments, owing to their high cost, are not readily accessible to all laboratories. Moreover, these characterizations are demanding, as they require relatively long-time analysis and careful data processing. Investigating the effects of annealing temperature or dopants on band positions, for example, can be challenging due to the extensive array of experiments required.

Theoretical methods serve as a valuable tool for calculating the CBM in the customized design of materials. In literature there are few works employing different ab-initio methods to calculate the absolute position of the SnO_2 conduction band.[41–43] Min et al.[42] extracted a value of −5.1 eV using PBE0 level of theory, spin-orbit orbit coupling, and TS dispersion correction, aligning the Hartree potential of the SnO_2 slab with that of the SnO_2/perovskite interface. Sopiha et al.[43] calculated energies of the band edges by adjusting in-plane average potential in the middle of the vacuum slab to zero. A CBM value of about −6.2 eV was obtained using PBE with Hubbard (U) correction ($U = 3.5$ or 4.7 eV) or HSE06 exchange-correlation functionals. Das et al.[41] developed a semi-empirical approach named the "Helium-slab approach." By utilizing an optimized Hartree-Fock exact-exchange parameter of 73%, extracted from a least-squares fit procedure on experimental data from various materials, the proposed approach successfully simulated the experimental band edges of SnO_2 and other materials. However, prior to applying the fitting procedure, they predicted values of −1.9 and −2.9 eV for the CBM, respectively, at PBE and HSE06 level of theory, well above the upper limit of the experimental range. As a matter of fact, the predicted band edges of SnO_2, as determined at the current state of the art through ab-initio methods, fall outside the experimentally measured range.

Here, we apply an effective computational scheme designed to calculate the CBM values of stannic oxide, yielding results well aligned with experimental measurements. We prove the fundamental role played by surface oxygen vacancies in reproducing experimental band edge values. We simulate the average experimental surface-vacancy concentration in literature (33%) assessing the impact of the V_{OP}:V_{OB} ratios on the conduction band edge position. We use the intrinsic surface oxygen vacancy formation energy (E_{vac}), as discerning criterion among the different possible scenarios. Our results predict ratios in line with experimental observation to be the most stable ones, with predicted CBM lying in the experimental range. On the contrary, the configuration with only V_{OB}, although energetically favorable as well, provides a CBM outside the experimental range present in literature, enforcing the need of simulate both types of surface defects.

This study represents a further step toward the effective modeling of the electronic properties of SnO_2, enhancing our understanding of factors influencing the conduction band edge position. Our findings can support experimental efforts toward a tailored functionalization of SnO_2 for technological applications.

2 | METHODS AND COMPUTATIONAL DETAILS

We build the pristine (110) SnO_2 slab starting from the optimized SnO_2 bulk structure obtained in a previous work.[44] The choice of the exposed facet is motivated by experimental and theoretical studies that identify the (110) surface as the most stable in rutile structure.[22,23] The slab model, shown in Figure S2, is thick 15 layers (5 tri-layers O–Sn–O) and contains 180 ions. Our surface model consists of a 3 × 2 supercell of the (110) unit cell. The thickness of the slab has been chosen from a convergence test that ensures the correct simulations of the bulk properties. The vacuum space is large enough (10 Å) to avoid interactions between the slabs repeated in the z-direction. The slab contains 6 bridging and 12 in-plane oxygens on each surface. This size allows us to explore different oxygen defective V_{OP}:V_{OB} configurations. Our study focuses on systems with 33% of surface oxygen vacancies, as it is a mean value of the range found experimentally.[24–26] This content was achieved by removing 6 of 18 surface oxygen ions. Our defective slab models are symmetric on both sides so to prevent a fictitious dipole formation. Oxygen vacancy positions on each surface are selected via the Special Quasi-random Structure (SQS) approach, implemented through the sqsgenerator code,[45] in order to maximize the configurational entropy. The vacancy formation energy (E_{vac}) is calculated following the approach by Oviedo and Gillan[46]:

$$E_{vac} = \frac{E_{def} + \frac{1}{2}nE_{O_2} - E_{prist}}{n},$$

where E_{O_2} is the energy of the oxygen molecule, E_{def} and E_{prist} are the energies of the defective and pristine systems, respectively, and n is

the number of O vacancies in the model. This energy has been calculated at HSE06 level of theory. We perform a Bader charge analysis, as implemented by the Henkelman group,[47,48] to further elucidate our findings.

We calculate the CB edge energy position of the pristine SnO_2 material following the approach proposed by Toroker et al.[49] Briefly, the band gap centre (BGC) is obtained as the midpoint between highest occupied energy level and the lowest unoccupied energy level. The resultant BGC is then referenced to the vacuum energy calculated as the electrostatic potential in the vacuum region. Finally, the CBM is extracted by adding to this value half of the experimental band gap of SnO_2. We chose the bulk SnO_2 band gap value of 3.6 eV.[15,50] To extract the shifts of the CBM in oxygen-defective slabs, we subtract to the predicted CBM for the pristine slab, the WF difference between the defective and the pristine slabs (WF_{def} and WF_{prist}). We correct the WF_{prist} by subtracting its calculated band gap, to account for the n-type behavior of the material conferred by vacancies. Thus, the CB edge of the defective systems is obtained by means of the following formula:

$$\mathrm{CBM}\,(\mathrm{def}) = \mathrm{CBM}\,(\mathrm{prist}) - \left(\mathrm{WF_{def}} - \left(\mathrm{WF_{prist}} - \mathrm{BG_{prist}}\right)\right),$$

where $\mathrm{CBM}\,(\mathrm{prist})$ and $\mathrm{CBM}\,(\mathrm{def})$ are the absolute position of the CB in the pristine and defective systems, respectively, and WF_{prist} and WF_{def} their work functions defined as the difference between the vacuum energy and the highest occupied energy level.

We perform periodic spin-polarized density functional theory (DFT) calculations based on plane waves, as implemented in the VASP code (version 5.4.1). All the slab structures are relaxed within a threshold of 0.03 eV/Å. Plane wave energy cut-off was set at 600 eV in all calculations and the SC-loop break condition was set to 10^{-5} eV. Ionic cores are represented by projector-augmented wave (PAW) potentials[51,52]: $2s^2 2p^4$ electrons for O and $5s^2 5p^2$ electrons for Sn are treated as valence electrons. We use the Perdew, Burke, and Ernzerhof (PBE) GGA-exchange-correlation density functional[53,54] for structural optimizations, and single-point HSE06[55,56] calculations are performed on the optimized PBE structures. Dispersion energies are treated with the Grimme's D3 correction[57] with the damping scheme by Becke and Jhonson (D3BJ).[58] K-points grids used are Γ-centered Monkhorst-Pack. A $3 \times 3 \times 1$ mesh is employed for PBE and $2 \times 2 \times 1$ for HSE06 calculations, respectively.

3 | RESULTS AND DISCUSSION

We consider different V_{OP}:V_{OB} ratios, ranging from the all bridge (all the bridging O lost) to the all in-plane (six in-plane O are missed), and going through mixed in-plane/bridging oxygen vacancies configurations. The five considered configurations are schematically illustrated in Figure 1A.

The vacancy formation energy (E_{vac}) reaches its minimum in the 1:1 configuration, as shown in Figure 1. Increasing the number of in-plane vacancies provides higher energies for the 2:1 and the all in-plane configurations. Such a result is in line with the expected behavior since in-plane oxygens are more coordinated (3-fold coordination) than bridge ones (2-fold coordination) necessitating the breaking of more bonds to create the defect. As we progress to configurations with an excess of bridge vacancies (1:2 and all bridge) the calculated energies are unexpectedly higher than the 1:1 case, although containing a smaller number of in plane vacancies. The analysis of the structural and electronic features examined through a Bader charge analysis elucidate these, at first glance, anomalous findings. Table S1 summarizes the total gain in Bader charge for tin and oxygen atoms on the surface upon the formation of vacancies, while Figure 1b represents a detailed analysis of which tin atoms are involved in the charge gain, where the acquired charge is depicted as a gray halo. Notably, the corresponding charge variations on the remaining oxygens are approximately one order of magnitude smaller ($\sim 10^{-2}$ e), indicating that charge reorganization predominantly involves the metal atoms. It is important to highlight that, with a fixed number of oxygen vacancies, both configurations with 6 (1:1 and all bridge) and 7 reduced Sn^{2+} atoms are observed. This discrepancy arises from distinct compensation mechanisms: in 7-Sn^{2+} configurations, the compensation mainly involves surface Sn atoms, whereas in 6-Sn^{2+} configurations, it also encompasses surface oxygen atoms. This differential delocalization mechanism is corroborated by the Bader charge fluctuations for oxygen atoms, as presented in the last column of Table S1. Notably, the configurations with fewer reduced Sn atoms (1:1 and all bridge) exhibit the highest ΔBader values of 0.55 and 0.56, respectively. There is a significant correlation between the charge variation on Sn ions and vacancy formation energies, except for the all bridge configuration, which contains only six Sn^{2+} ions despite having an energy similar to the 1:2 configuration. The analysis suggests the reduction of surface tin atoms to be the reason of the higher energy values.

The deviation played by the all-bridge model can be explained by the peculiar "in row" charge localization (Figure 1) probably representing the reason for energy comparable with the 1:2 configuration. Conversely, the remaining configurations exhibit a more delocalized charge distribution.

A joint structural-electronic analysis reveals another effect occurring on the surface of some of the considered models. Upon the formation of the vacancies, some of the surface tin atoms change their coordination and both 4- and 3-fold coordinated metal atoms appear. In almost all cases a such change of the coordination is accompanied by a reduction of the involved atoms from Sn^{4+} to Sn^{2+}. In the mixed V_{OP}/V_{OB} configurations (2:1, 1:1, 1:2) a peculiar structural reorganization occurs in 4-fold coordinated tin atoms in which the more the oxygen coordination becomes tetrahedral, the more a delocalization effect occurs in which the atom keeps its +4 oxidation state. Such effect is shown in Figure S3 with the angles summarized in Table S2.

The theoretically predicted energy trends also point out the synergic role of both defect types in influencing the energy value. Oviedo and Gillan previously explored all in-plane and bridge oxygen-deficient configurations at varying concentrations of oxygen vacancies.[46] Their results affirm that under specific vacancy concentrations and geometrical configurations, it is feasible to achieve comparable E_{vac} for both defect

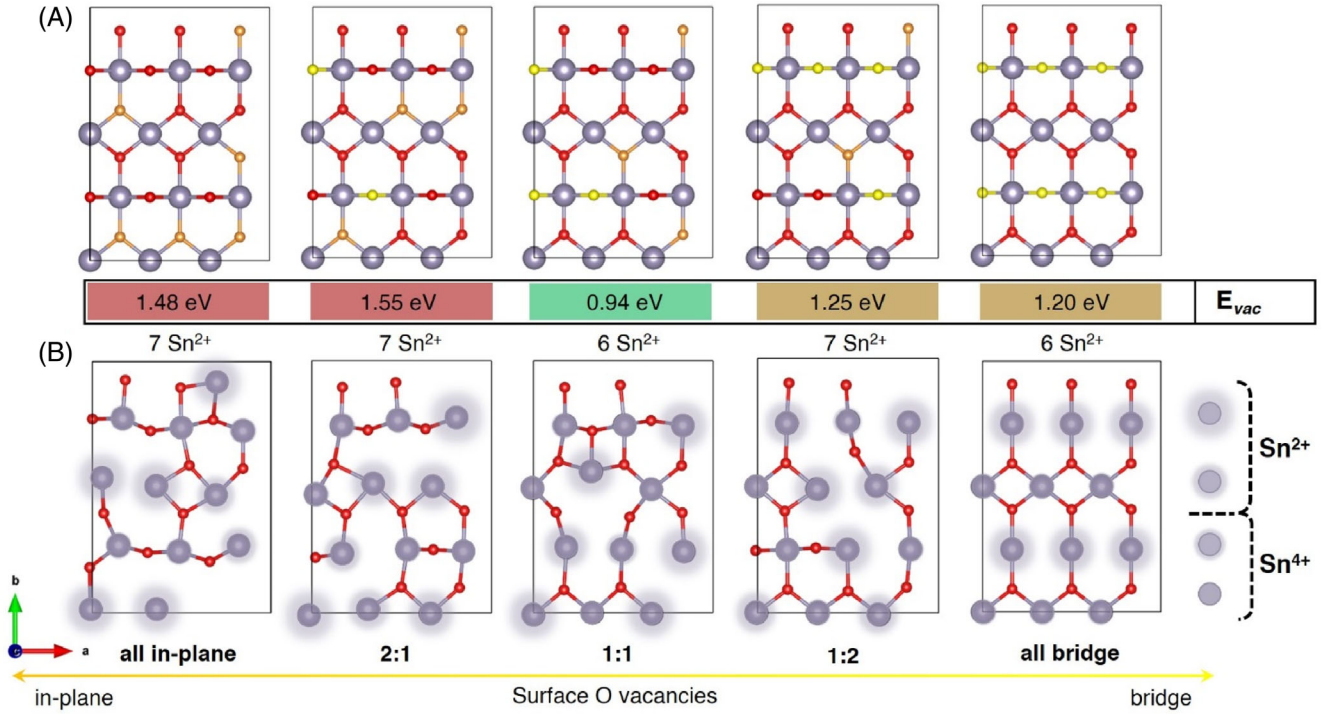

FIGURE 1 Top views of surfaces with different V_{OP}:V_{OB} ratios before (A) and after (B) geometry optimization. V_{OP} and V_{OB} are depicted in (A) as orange and yellow spheres, respectively; gray circles in (B) display the ΔBader charge associated with the Sn ions. The figure includes vacancy formation energy (E_{vac}) values and number of reduced Sn^{2+} ions for each configuration.

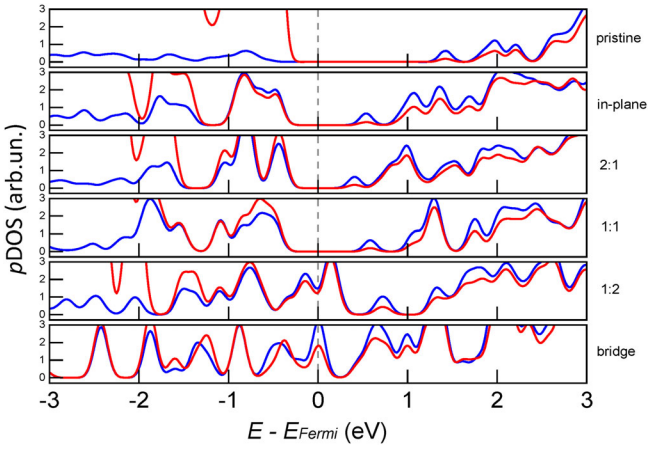

FIGURE 2 *p*DOS of systems containing different V_{OP}:V_{OB} ratios studied at HSE06 level of theory. The dashed line denotes the Fermi level. Color legend: Sn (s)—blue, O (p)—red.

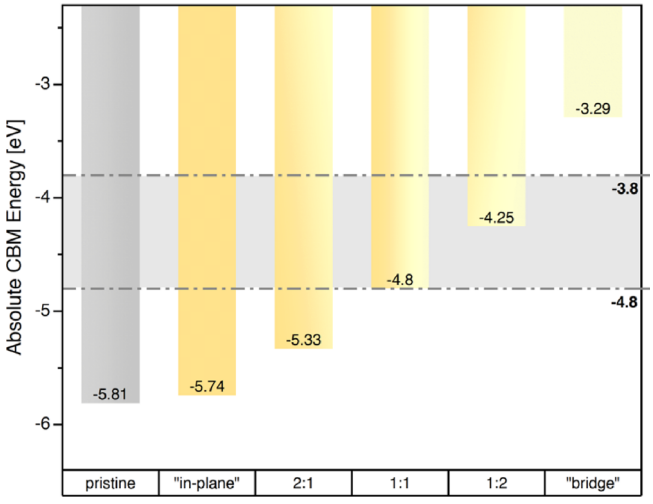

FIGURE 3 Absolute CB edge positions of pristine and defective SnO_2 surfaces computed at HSE06 level of theory. Pristine and defective configurations are colored, respectively, in gray and with a gradient from orange (all in-plane) to light yellow (all bridge). The experimental CBM interval[34–40] is denoted with a gray zone.

types. We investigate the configurations, named here (a) and (b), studied in this work at 33% using our level of theory (Figure S4). The observed energy trend in this study aligns with the results presented in Reference [46] (refer to Table S3). The in-plane configuration (a) exhibits a similar E_{vac} to the all bridge configuration, whilst the in-plane configuration (b) is higher in energy. This confirms that, within certain arrangements and geometries, both defect types are energetically comparable. The outcomes of the present study further elaborate on this concept, demonstrating the feasibility of attaining E_{vac} even lower than those associated with the all bridge. This is achieved through configurations that contain both types of vacancies.

We calculate the Projected-Density of States (*p*DOS), displayed in Figure 2 to further analyze the electronic properties of our models. The data clearly illustrate that the bandgap decreases or disappears when oxygen vacancies are introduced in the slab, as expected with

the creation of intra-gap levels.[30] As a result, the Fermi level shifts toward the conduction band. In particular, when the quantity of V_{OB} exceeds the number of in-plane oxygen vacancies, the disappearance of the bandgap suggests a significant increase in free charge carriers due to this type of vacancies.

We evaluate the positions of the CBM both for the pristine and the defective models following the procedure described in the previous section. In Figure 3 are depicted the obtained values calculated at HSE06 level of theory. Notably the value extracted from the pristine model (−5.81 eV) falls well outside the experimental range. In defective systems, it is possible to observe that the higher the content of bridging oxygen vacancies, the higher the CBM. On one side the all in-plane and the 2:1 configurations underestimate the experimental values, while on other the all bridge configuration provides a too high energy value. The 1:1 and 1:2 configurations provide instead values in the experimental range of CBM. These configurations are also among the most energetically favorable with ratios reflecting experimental values.[24,27]

4 | CONCLUSIONS

The present work employs periodic spin-polarized DFT calculations to assess the impact of surface oxygen vacancies on the structural and electronic features of stannic oxide. Such investigation is crucial for understanding and optimizing the performance of this n-type semiconductor, in applications such as perovskite solar cells, catalysis, and gas sensors. Herein, we have provided a comprehensive analysis of different V_{OP}:V_{OB} ratios, all containing 33% of surface oxygen vacancies, shedding light on their impact on vacancy formation energy (E_{vac}) and CBM positions.

Our results point out that configurations containing both defect types can be even more favorable than the all bridge configuration, despite the formation of oxygen bridge vacancies implies the breaking of less bonds.

The Bader charge analysis reveals that energy is influenced not only by surface tin reduction upon defect formation but also by the charge distribution.

Furthermore, this study emphasizes the correlation between the stability of surface configurations and the resulting CBM positions. A notable shift in CBM with varying V_{OP}:V_{OB} ratios is observed, demonstrating the interplay between surface defects and electronic structure. The CBM of the pristine structure falls well outside the experimental range value. By accounting for defects, we find a competing effect of in-plane and bridge vacancies to lower and increase the CBM position, respectively. This leads to results outside the experimental range for all the defective configurations, except for the 1:1 and the 1:2. Among the investigated configurations, these have some of the lowest E_{vac}. The results explain from an atomistic perspective the PL experimental results,[24,27] where SnO_2 surfaces containing a similar amount of $V_{OP} \sim V_{OB}$ or an excess of V_{OB} have been observed.

Further investigation of the electronic structure via pDOS analysis predicts a strong relation between the presence of oxygen vacancies and the material's conductivity, aligning with current literature. Our results reveal the predominant role of bridge vacancies to increase the conduction features.

In conclusion, this research contributes to advancing the understanding of factors influencing the conduction band edge position in SnO_2, offering a guidance for experimental efforts in functionalizing SnO_2 for diverse technological applications. The study underscores the importance of simulating both type of surface defects for accurately predicting the electronic and structural properties of the material. Moreover, this work provides a theoretical prescription serving as a roadmap for effective theoretical simulation of stannic oxide properties, especially these findings offer fundamental insights for future studies of interfacial features with other materials or manipulations, such as doping, or new fabrication processes.

ACKNOWLEDGMENTS

This study was carried out within the NEST—Network for Energy Sustainable Transition and received funding from the European Union Next-Generation EU (PIANO NAZIONALE DI RIPRESA E RESILIENZA (PNRR)—MISSIONE 4 COMPONENTE 2, INVESTIMENTO 1.3). This manuscript reflects only the authors' views and opinions, neither the European Union nor the European Commission can be considered responsible for them. The computing resources and the related technical support used for this work have been provided by CRESCO/ENEAGRID High Performance Computing infrastructure and its staff[59]; CRESCO/ENEAGRID High Performance Computing infrastructure is funded by ENEA, the Italian National Agency for New Technologies, Energy and Sustainable Economic Development and by Italian and European research programs, see http://www.cresco.enea.it/english for information.

DATA AVAILABILITY STATEMENT

The data that support the findings of this study are available from the corresponding author upon reasonable request.

REFERENCES

[1] M. Kimura, *Jpn. J. Appl. Phys.* **2019**, *58*, 090503.
[2] X. Yu, T. J. Marks, A. Facchetti, *Nat. Mater.* **2016**, *15*, 383.
[3] G. S. Chae, *Jpn. J. Appl. Phys.* **2001**, *40*, 1282.
[4] M. Tiemann, *Chem. A Europ. J.* **2007**, *13*, 8376.
[5] C. Wang, L. Yin, L. Zhang, D. Xiang, R. Gao, *Sensors* **2010**, *10*, 2088.
[6] M. Patel, H.-S. Kim, J. Kim, *Adv. Electron. Mater.* **2015**, *1*, 1500232.
[7] T. Zhai, X. Fang, M. Liao, X. Xu, H. Zeng, B. Yoshio, D. Golberg, *Sensors* **2009**, *9*, 6504.
[8] I. Concina, A. Vomiero, *Small* **2015**, *11*, 1744.
[9] K. Valadi, S. Gharibi, R. Taheri-Ledari, S. Akin, A. Maleki, A. E. Shalan, *Environ. Chem. Lett.* **2021**, *19*, 2185.
[10] G. V. Sannino, A. De Maria, V. La Ferrara, G. Rametta, L. V. Mercaldo, M. L. Addonizio, L. Lancellotti, A. Pecoraro, A. B. Muñoz-García, M. Pavone, P. Delli Veneri, *Solids* **2021**, *2*, 407.
[11] S. R. Thomas, P. Pattanasattayavong, T. D. Anthopoulos, *Chem. Soc. Rev.* **2013**, *42*, 6910.
[12] Y. J. Jang, J. S. Lee, *ChemSusChem* **2019**, *12*, 1835.
[13] B. Zhang, Q. Ru, L. Liu, J. Wang, Y. Zhang, K. Zhao, G. Gu, X. Xiang, S. Li, Y. Zhu, Y. Jia, G. Cheng, Z. Du, *J. Catal.* **2023**, *419*, 1.
[14] J. C. Védrine, *Catalysts* **2017**, *7*, *341*.
[15] S. Das, V. Jayaraman, *Prog. Mater. Sci.* **2014**, *66*, 112.
[16] L. Xiong, Y. Guo, J. Wen, H. Liu, G. Yang, P. Qin, G. Fang, *Adv. Funct. Mater.* **2018**, *28*, 1802757.

[17] L. Villamagua, A. Stashans, P.-M. Lee, Y.-S. Liu, C.-Y. Liu, M. Carini, *Chem. Phys.* **2015**, *452*, 71.
[18] C. Guillén, J. Herrero, *J. Alloys Compd.* **2019**, *791*, 68.
[19] K. G. Godinho, A. Walsh, G. W. Watson, *J. Phys. Chem. C* **2009**, *113*, 439.
[20] J. Liu, S. Li, S. Liu, Y. Chu, T. Ye, C. Qiu, Z. Qiu, X. Wang, Y. Wang, Y. Su, Y. Hu, Y. Rong, A. Mei, H. Han, *Angew. Chem., Int. Ed.* **2022**, *61*, e202202012.
[21] S. Samson, C. G. Fonstad, *J. Appl. Phys.* **2003**, *44*, 4618.
[22] J. Oviedo, M. J. Gillan, *Surf. Sci.* **2000**, *463*, 93.
[23] Y. Duan, *Phys. Rev. B* **2008**, *77*, 045332.
[24] V. Bonu, A. Das, A. K. Prasad, N. G. Krishna, S. Dhara, A. K. Tyagi, *Appl. Phys. Lett.* **2014**, *105*, 243102.
[25] N. Luo, C. Wang, D. Zhang, M. Guo, X. Wang, Z. Cheng, J. Xu, *Sens. Actuators, B* **2022**, *354*, 130982.
[26] Y. Xu, L. Zheng, C. Yang, W. Zheng, X. Liu, J. Zhang, *ACS Appl. Mater. Interfaces* **2020**, *12*, 20704.
[27] S. Deepa, K. Prasanna Kumari, B. Thomas, *Ceram. Int.* **2017**, *43*, 17128.
[28] Y. Ai, W. Liu, C. Shou, J. Yan, N. Li, Z. Yang, W. Song, B. Yan, J. Sheng, J. Ye, *Solar Energy* **2019**, *194*, 541.
[29] A. Ahmed, M. Naseem Siddique, U. Alam, T. Ali, P. Tripathi, *Appl. Surf. Sci.* **2019**, *463*, 976.
[30] D. Toloman, A. Popa, M. Stefan, T. D. Silipas, R. C. Suciu, L. Barbu-Tudoran, O. Pana, *Opt. Mater.* **2020**, *110*, 110472.
[31] M. F. Mohamad Noh, N. A. Arzaee, J. Safaei, N. A. Mohamed, H. P. Kim, A. R. Mohd Yusoff, J. Jang, M. A. Mat Teridi, *J. Alloys Compd.* **2019**, *773*, 997.
[32] M. Epifani, J. D. Prades, E. Comini, E. Pellicer, M. Avella, P. Siciliano, G. Faglia, A. Cirera, R. Scotti, F. Morazzoni, J. R. Morante, *J. Phys. Chem. C* **2008**, *112*, 19540.
[33] Q. Liu, H. Zhan, X. Huang, Y. Song, S. He, X. Li, C. Wang, Z. Xie, *Eur. J. Inorg. Chem.* **2021**, *2021*, 4370.
[34] S. Akin, *ACS Appl. Mater. Interfaces* **2019**, *11*, 39998.
[35] Q. Guo, J. Wu, Y. Yang, X. Liu, Z. Lan, J. Lin, M. Huang, Y. Wei, J. Dong, J. Jia, Y. Huang, *Research* **2019**, *2019*, 4049793.
[36] Z. Li, R. Wang, J. Xue, X. Xing, C. Yu, T. Huang, J. Chu, K.-L. Wang, C. Dong, Z. Wei, Y. Zhao, Z.-K. Wang, Y. Yang, *J. Am. Chem. Soc.* **2019**, *141*, 17610.
[37] M. Park, J.-Y. Kim, H. J. Son, C.-H. Lee, S. S. Jang, M. J. Ko, *Nano Energy* **2016**, *26*, 208.
[38] Y. Sun, Z. Pang, Y. Quan, D. Han, X. Zhang, X. Ge, F. Wang, Y. Sun, J. Yang, L. Yang, *Chem. Eng. J.* **2021**, *413*, 127387.
[39] J. Wang, K. Datta, C. H. L. Weijtens, M. M. Wienk, R. A. J. Janssen, *Adv. Funct. Mater.* **2019**, *29*, 1905883.
[40] S. Huang, Y. Tang, A. Yu, Y. Wang, S. Shen, B. Kang, S. R. P. Silva, G. Lu, *Org. Electron.* **2018**, *62*, 373.
[41] T. Das, X. Rocquefelte, S. Jobic, *J. Phys. Chem. C* **2020**, *124*, 19426.
[42] H. Min, D. Y. Lee, J. Kim, G. Kim, K. S. Lee, J. Kim, M. J. Paik, Y. K. Kim, K. S. Kim, M. G. Kim, T. J. Shin, S. Il Seok, *Nature* **2021**, *598*, 444.
[43] K. V. Sopiha, O. I. Malyi, C. Persson, P. Wu, *ACS Appl. Mater. Interfaces* **2021**, *13*, 33664.
[44] G. V. Sannino, A. Pecoraro, P. Maddalena, A. Bruno, P. D. Veneri, M. Pavone, A. B. Muñoz-García, *Sustain. Energy Fuels* **2023**, *7*, 4855.
[45] D. Gehringer, M. Friák, D. Holec, *Comput. Phys. Commun.* **2023**, *286*, 108664.
[46] J. Oviedo, M. J. Gillan, *Surf. Sci.* **2000**, *467*, 35.
[47] W. Tang, E. Sanville, G. Henkelman, *J. Phys. Condens. Matter* **2009**, *21*, 084204.
[48] M. Yu, D. R. Trinkle, *J. Chem. Phys.* **2011**, *134*, 064111.
[49] M. C. Toroker, D. K. Kanan, N. Alidoust, L. Y. Isseroff, P. Liao, E. A. Carter, *Phys. Chem. Chem. Phys.* **2011**, *13*, 16644.
[50] M. M. Bagheri-Mohagheghi, N. Shahtahmasebi, M. R. Alinejad, A. Youssefi, M. Shokooh-Saremi, *Phys. B* **2008**, *403*, 2431.
[51] P. E. Blöchl, *Phys. Rev. B* **1994**, *50*, 17953.
[52] G. Kresse, D. Joubert, *Phys. Rev. B* **1999**, *59*, 1758.
[53] J. P. Perdew, K. Burke, M. Ernzerhof, *Phys. Rev. Lett.* **1996**, *77*, 3865.
[54] J. P. Perdew, K. Burke, M. Ernzerhof, *Phys. Rev. Lett.* **1997**, *78*, 1396.
[55] J. Heyd, G. E. Scuseria, M. Ernzerhof, *J. Chem. Phys.* **2003**, *118*, 8207.
[56] J. Heyd, G. E. Scuseria, M. Ernzerhof, *J. Chem. Phys.* **2006**, *124*, 219906.
[57] S. Grimme, S. Ehrlich, L. Goerigk, *J. Comput. Chem.* **2011**, *32*, 1456.
[58] A. D. Becke, E. R. Johnson, *J. Chem. Phys.* **2005**, *123*, 154101.
[59] G. Ponti, F. Palombi, D. Bate, F. Ambrosino, G. Aprea, T. Bastianelli, F. Beone, B. Calosso, M. Chinnici, A. Colavincenzo, A. Cucurullo, P. Dangelo, M. De Michele, A. Funel, A. Italiano, S. Magagnino, A. Mariano, G. Mencuccini, C. Mercuri, S. Migliori, P. Ornelli, S. Pecoraro, A. Perozziello, S. Pierattini, S. Podda, F. Poggi, A. Quintiliani, A. Rocchi, C. Sciò, F. Simoni, A. Vita, *International Conference on High-Performance Computing & Simulation (HPCS)*, IEEE, Bologna, Italy **2014**, p. 1030.

SUPPORTING INFORMATION

Additional supporting information can be found online in the Supporting Information section at the end of this article.

How to cite this article: G. V. Sannino, A. Pecoraro, P. D. Veneri, M. Pavone, A. B. Muñoz-García, *J. Comput. Chem.* **2024**, *45*(26), 2198. https://doi.org/10.1002/jcc.27434